Journal of The Korean Astronomical Society
45: 71 ∼ 84, 2012 June

http://dx.doi.org/10.5303/JKAS.2012.45.3.71
ISSN:1225-4614
http://jkas.kas.org

WASHINGTON PHOTOMETRY OF THE GLOBULAR CLUSTERS IN THE VIRGO GIANT ELLIPTICAL GALAXY M86

Hong Soo Park
Department of Physics and Astronomy, Seoul National University, Seoul 151-742, Korea
E-mail : hspark@astro.snu.ac.kr
(Received May 10, 2012; Revised May 24, 2102; Accepted May 28, 2012)

ABSTRACT

We present a photometric study of the globular clusters (GCs) in the Virgo giant elliptical galaxy M86 based on Washington CT_1 images. The colors of the GCs in M86 show a bimodal distribution with a blue peak at $(C-T_1)=1.30$ and a red peak at $(C-T_1)=1.72$. The spatial distribution of the red GCs is elongated similar to that of the stellar halo, while that of the blue GCs is roughly circular. The radial number density profile of the blue GCs is more extended than that of the red GCs. The radial number density profile of the red GCs is consistent with the surface brightness profile of the M86 stellar halo. The GC system has a negative radial color gradient, which is mainly due to the number ratio of the blue GCs to the red GCs increasing as galactocentric radius increases. The bright blue GCs in the outer region of M86 show a blue tilt: the brighter they are, the redder their mean colors get. These results are discussed in comparison with other Virgo giant elliptical galaxies.

Key words : galaxies: clusters — galaxies: individual (M86, NGC 4406) — galaxies: photometry — galaxies: star clusters

1. INTRODUCTION

Thousands of globular clusters (GCs) are found in a giant elliptical galaxy (gE) and they are found to be located from the center to the outer halo of their host galaxy (Lee 2003; Brodie & Strader 2006). Therefore, the GCs in gEs are a powerful tool to study the structure and evolution of the GC system itself as well as their host galaxy.

M86 (NGC 4406, VCC 881) is a famous gE located close to the center region of the Virgo galaxy cluster in the sky and is known to be infalling to the Virgo center with the relative velocity of about 1300 km s^{-1}. It is also known early to be abundant with GCs (Hanes 1977). There are several photometric studies for the GCs in M86 in the literature. Cohen (1988) presented *gri* photometry of GCs at $R<7'$ in M86 obtained at the Hale 5 m telescope. She found that the GC system of M86 is similarly extended as the stellar light, and that there is no detectable radial color gradient.

From HST/WFPC2 VI observation of the central region of M86, Neilsen & Tsvetanov (1999) reported that the color distribution of the GCs in M86 shows a single peak. However, Kundu & Whitmore (2001) and Larsen et al. (2001) showed later, using the same data as used in HST/WFPC2 by Neilsen & Tsvetanov (1999), that the color distribution of the GCs in M86 is bimodal. Later Peng et al. (2006) confirmed, from HST/ACS *gz* observation, that the color distribution of M86 GCs is bimodal.

Jordán et al. (2009) and Villegas et al. (2010) derived a luminosity function of M86 GCs from the same HST/ACS images, and obtained a similar Gaussian peak value at *g*-band, $\mu_g = 23.950 \pm 0.097$ and 23.887 ± 0.087, respectively. Peng et al. (2008) estimated the specific frequency of M86 GCs, $S_N = 2.57 \pm 0.12$, from the HST/ACS images. On the other hand, Rhode & Zepf (2004) investigated M86 GCs using the wide field ($36' \times 36'$) BVR images obtained using the KPNO 4 m Mayall telescope. They found again that M86 GCs show a bimodal color distribution and that they show a modest negative color gradient with galactocentric radius. They derived a specific frequency of $S_N = 3.5 \pm 0.5$, which is larger than the value derived from the central region by Peng et al. (2008).

However, previous studies based on HST data covered only a small central region of M86 and those based on ground-based data did not investigate the properties of sub-populations in the GC system and the spatial distribution of the GCs in M86. Here we investigate the detailed properties of the M86 GC system using Washington photometry derived from deep and wide CCD images. The Washington filter system with a wide bandwidth is known to be very sensitive to measuring the metallicity of the GCs (Geisler & Forte 1990) so that it is useful for studying the properties of sub-populations of the GCs. We adopt a distance to M86, derived from the surface brightness fluctuation method by Mei et al. (2007), 16.9 Mpc ($(m-M)_0 = 31.13 \pm 0.07$). At this distance one arcsec corresponds to a linear scale of 81 pc. The basic information of M86 is listed in Table 1.

This paper is composed as follows. Section 2 describes observations and data reduction. In section 3, we present the color-magnitude diagram and color distribution of the M86 GCs. We investigate the spatial distribution of the GC system as well as the radial variation of number densities and colors of the GCs. In section 4, we discuss our results and their implication in comparison with other Virgo gE studies. Primary results are summarized in section 5.

2. OBSERVATION AND DATA REDUCTION

2.1 Observations

The images of M86 were obtained with the 2048 × 2048 pixels CCD camera (the pixel scale is 0.47 arcsec pixel^{-1}) at the KPNO 4 m telescope on the photometric night of April 9, 1997. These images were taken with the Washington C and Kron-Cousins R filters. The R filter was used instead of the Washington T_1 filter, as done in most recent Washington studies (Geisler 1996; Lee et al. 1998; Harris et al. 2004; Dirsch et al. 2005; Bassino et al. 2006; Forte et al. 2007; Lee et al. 2008), because the sensitivity of the Kron-Cousins R filter is about three times larger than that of the T_1 filter, while the effective wavelengths of two filters are very similar as $R = T_1 + 0.003 - 0.017(C - T_1)$ with rms=0.02 Geisler (1996). Hereafter we call this R filter as T_1 filter in the rest of this paper.

Table 2 shows the observation log. The size of the field of view is $16' \times 16'$, and the seeing range is from $1''.0$ to $1''.2$. Exposure times are 60 s and 4×1500 s for C, and 30 s and 2×1000 s for T_1. Several Washington standard fields in Geisler (1996) were also observed during the observing run.

2.2 Point Source Photometry

Using the IRAF software, each frame was bias-subtracted and flat-fielded. Then the long exposure images of two T_1-bands and four C-bands were combined with average and median procedure, respectively. Fig. 1 displays a T_1 image of M86 taken with the short exposure.

The GCs at the M86 distance appear as point sources in the KPNO images so that we derived photometry of the point sources from the images as follows. First, we derived isophotal model images of M86 with ELLIPSE task in IRAF/STSDAS. Then we subtracted these images from the original images to detect better point sources in the images. Next we carried out the point-spread function (PSF) photometry on the subtracted images using the DAOPHOT/ALLFRAME (Stetson 1994). Then we derived the aperture correction using the photometry of several isolated bright stars and applied it to the PSF-fitting magnitudes: 0.013 ± 0.006 and 0.019 ± 0.004 for short and long exposure C images and -0.025 ± 0.008 and 0.022 ± 0.003 for short and long exposure T_1 images. Finally, we transformed the instrumental magnitudes of the sources onto the standard system using the transformation equations (April 9) given in section 2.3 by Lee et al. (2008). We selected the point sources among the detected sources using the morphological classifier r_{-2} moment Kron (1980). We considered the sources with $r_{-2} < 1.27$ as the point sources. Fig. 2 displays the mean errors of T_1 and $(C - T_1)$ versus T_1 magnitude, and Table 3 lists the CT_1 photometry catalog of only 4351 point sources with error $(C - T_1) < 0.3$ measured in the KPNO images.

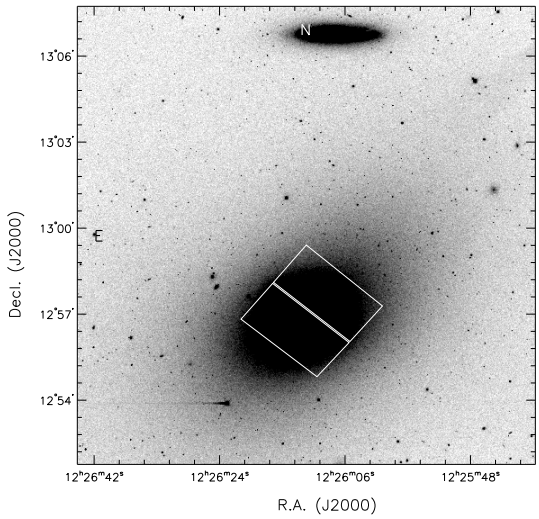

Fig. 1.— A grey scale map of T_1 image of the M86 field taken with KPNO 4 m telescope. The field of view is $16' \times 16'$. The boxes represent the HST/ACS fields. The galaxy in the north is NGC 4402, which is an edge-on galaxy of Sb type.

The central region at $R \lesssim 1$ arcmin in the long exposure images was saturated and the short exposure images are too shallow. Therefore, we used HST photometry available in Jordán et al. (2009) for the analysis of the central region of M86. Jordán et al. (2009) provides a photometric catalog of GCs in 100 early-type galaxies in Virgo including M86, derived from the HST/ACS Virgo Cluster Survey (ACSVCS). Their catalog includes g and z magnitudes, and the probability for GC classification ($p_{\rm GC}$). GCs appear as extended objects in the ACS images and the sources with $p_{\rm GC} > 0.5$ are considered as GC candidates.

We derived the transformation between $(C - T_1)$ colors and $(g - z)$ colors for the bright objects (with $T_1 < 22.0$ mag, error $(C - T_1) < 0.08$ and $1.1 < (C - T_1) < 2.1$), using the common objects between the KPNO results and the ACSVCS catalog. Fig. 3 shows the relations for colors and magnitudes. There are several outliers, which are due to being located near saturated sky levels or having nearby sources. We fitted the data after excluding these outliers. Linear fitting to the data yields $(g - z) = 0.773(C - T_1) - 0.118$ with rms=0.068, and $g = 0.998T_1 + 0.911$ with rms=0.109.

Table 1.
Basic information on M86

Parameters	Values	References
R.A., Decl. (J2000)	$12^h\ 26^m\ 11.743^s$, $+12^\circ\ 56'\ 46.40''$	1
Total magnitudes	$V^T = 8.90 \pm 0.05$, $B^T = 9.83 \pm 0.05$	2
Foreground reddening, $E(B-V)$	0.030	3
Distance, d	16.86 Mpc ($(m-M)_0 = 31.13 \pm 0.07$)	4
Systemic radial velocity, v_p	-244 ± 5 km s^{-1}	5
Effective radius, R_{eff}	3.59 arcmin (C), 3.14 arcmin (T_1)	6
Effective ellipticity, ϵ_{eff}	0.36 (C), 0.33 (T_1)	6
Effective P.A., Θ_{eff}	119 deg (C, T_1)	6
Standard radius, R_{25}	4.88 arcmin (C), 9.64 arcmin (T_1)	6
Standard ellipticity, ϵ_{25}	0.40 (C, T_1)	6
Standard P.A., Θ_{25}	124 deg (C, T_1)	6

REFERENCES.—(1) NASA Extragalactic Database; (2) de Vaucouleurs et al. (1991); (3) Schlegel et al. (1998); (4) Mei et al. (2007); (5) Smith et al. (2000); (6) This study.

Table 2.
Observation log

Target	Filter	T(exp) (sec)	Airmass	Seeing ($''$)	Date (UT)
M86	C	60	1.12	1.13	1997 Apr 9
M86	R	30	1.06	0.99	1997 Apr 9
M86	C	4×1500	1.06	1.13	1997 Apr 9
M86	R	2×1000	1.21	1.22	1997 Apr 9

Table 3.
A catalog of Washington photometry for the point sources in M86[a]

ID	R.A. (J2000)	Decl. (J2000)	T_1±error (mag)	$(C-T_1)$±error (mag)
1	12:26:21.75	12:52:40.7	17.746 ± 0.011	2.883 ± 0.033
2	12:26:03.70	12:59:57.5	17.888 ± 0.023	2.750 ± 0.030
4	12:26:13.36	13:05:11.7	17.992 ± 0.010	0.777 ± 0.015
5	12:26:28.38	13:00:52.8	18.045 ± 0.014	0.792 ± 0.025
6	12:26:17.03	13:06:00.4	18.195 ± 0.011	2.163 ± 0.022
.....				

[a]The complete version of this table is in the electronic edition of the Journal. The printed edition contains only a sample.

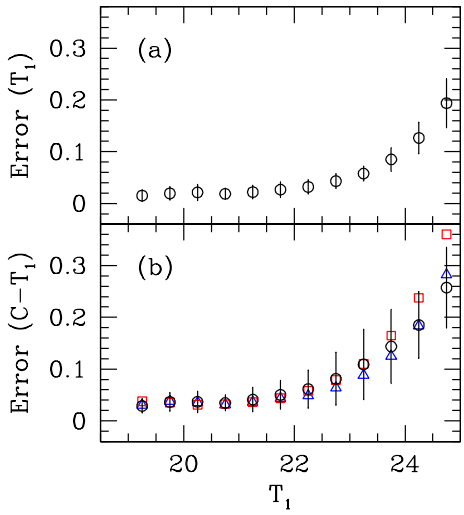

Fig. 2.— Mean photometric errors of T_1 magnitude and $(C-T_1)$ color for the point sources obtained from the long exposure images. The circles with error bars, triangles, and squares represent the mean errors of all point sources, the blue GCs ($1.0 < (C-T_1) < 1.55$), and the red GCs ($1.55 < (C-T_1) < 2.1$), respectively.

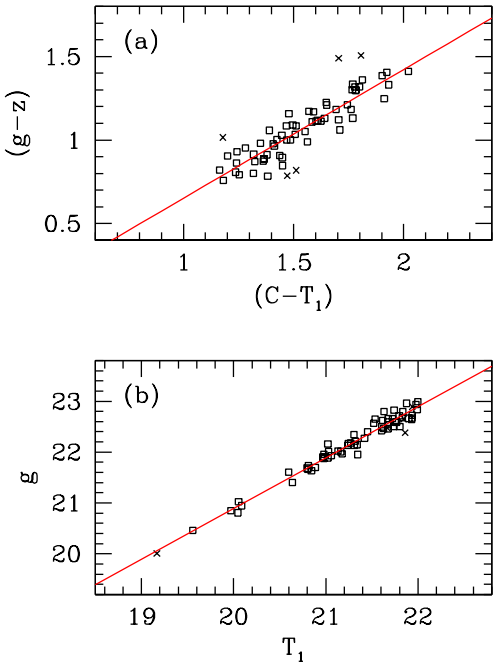

Fig. 3.— Comparison of $(C-T_1)$ with $(g-z)$ (a) and T_1 magnitude with g magnitude (b). The solid lines represent the linear least-squares fits for error $(C-T_1) < 0.08$ and $T_1 < 22.0$, except for the outliers indicated by the crosses.

2.3 Completeness of the Photometry

We estimated the completeness of the KPNO photometry using DAOPHOT/ADDSTAR, which is designed for the artificial star experiment. Firstly, we generated a set of artificial stars whose color-magnitude diagrams and luminosity functions are similar to those of the detected point sources, using the PSFs derived from the long exposure images. Next we added them to the real image avoiding the position of detected real sources. We obtained 50 artificial images, each of which includes 1200 artificial stars for each filter so that the total number of added artificial stars is 60,000. We applied the same photometry procedure to the artificial images as used for the real image. From these results, we estimated the completeness, which is the number ratio of the recovered artificial stars to the added artificial stars.

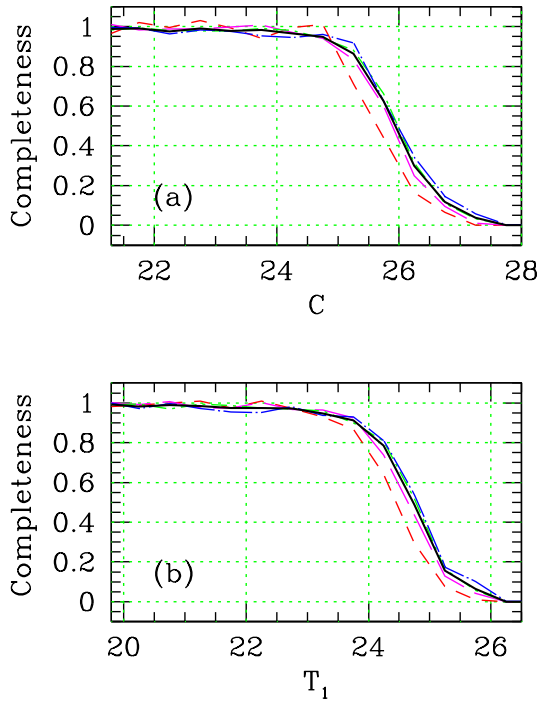

Fig. 4.— Completeness of C magnitude (a) and T_1 magnitude (b). The solid lines represent the results for the entire region. The short dashed, long dashed, dot-short dashed, and dot-long dashed lines indicate the completeness at $1' < R < 3'$, $3' < R < 5'$, $5' < R < 7'$, and $7' < R < 9'$, respectively.

Fig. 4 displays the completeness of C and T_1 magnitude measured for the point sources. This figure shows the completeness for the entire region and four radial bins: $1' < R < 3'$, $3' < R < 5'$, $5' < R < 7'$, and $7' < R < 9'$. The 90% completeness is located at $T_1 = 23.8$ ($C = 25.1$) for the outer region at $R > 3'$ and $T_1 = 23.5$ ($C = 24.9$) for the inner region at $1' < R < 3'$. The photometric limit levels with 50% completeness are $T_1 = 24.7$ ($C = 25.9$) for the outer region at $R > 3'$ and $T_1 = 24.4$ ($C = 25.6$) for the inner region at $1' < R < 3'$. The completeness varies little, depending on galactocentric radius for the outer region at $R > 3'$, while it is somewhat lower for the inner region at $R < 3'$ compared with the outer region.

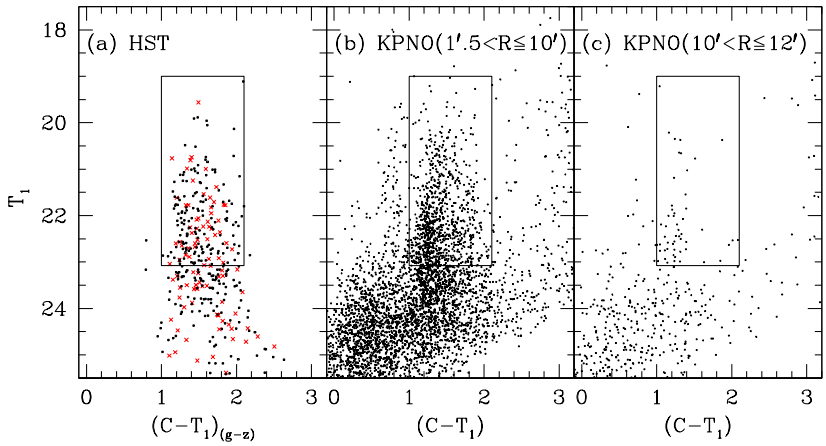

Fig. 5.— Color-magnitude diagrams of the sources in M86 given in ACSVCS catalog (a) and the point sources in M86 measured from the KPNO images (b and c). The boxes indicate the color ($1.0 < (C - T_1) < 2.1$) and magnitude ($19 < T_1 < 23.08$) criteria for selecting the M86 GCs. The dotted and crosses in panel (a) represent the values converted from g and $(g - z)$ at $R < 1'.5$ and $1'.5 < R < 2'.4$, respectively.

3. RESULTS

3.1 Color-Magnitude Diagram

Fig. 5 displays the color-magnitude diagrams (CMDs) of the point sources measured from the KPNO images of M86 as well as that from the HST/ACS photometry (for $R < 1'.5$). We plotted the CMDs for the M86 region ($1'.5 < R < 10'$) and the background region ($10' < R < 12'$). For the central region at $R < 1'.5$ we plotted only the HST photometry. We transformed the $(g - z)$ colors and g magnitudes of the objects given in the ACSVCS catalog into $(C-T_1)$ colors and T_1 magnitudes, respectively, using the transformation equations derived in the previous section.

Three distinct features are seen in Fig. 5: (a) GCs of M86 in the broad vertical feature in the color range of $1.0 < (C - T_1) < 2.1$, (b) a small number of bright foreground stars at $(C - T_1) \lesssim 1.0$ and $(C - T_1) \gtrsim 2.5$, and (c) faint blue unresolved background galaxies with $T_1 > 23$ mag. We selected the bright point sources with $1.0 < (C - T_1) < 2.1$ and $19 < T_1 < 23.08$ for the analysis of the M86 GCs, considering the following points: (1) the color range of the known GCs in other galaxies is $(C - T_1) \approx 0.9$ to 2.1 (Geisler 1996; Lee et al. 1998; Dirsch et al. 2005; Forte et al. 2007; Lee et al. 2008); (2) the peak luminosity of the M86 GCs is $T_1 = 23.08$, which was converted from the peak g magnitude ($\mu_g = 23.95 \pm 0.10$) given by Jordán et al. (2007); (3) the mean photometric error and the completeness for $T_1 < 23.08$ are smaller than error $(T_1) = 0.05$ and larger than 90%, respectively; and (4) the contamination due to background galaxies is estimated to be very small for $T_1 < 23.08$.

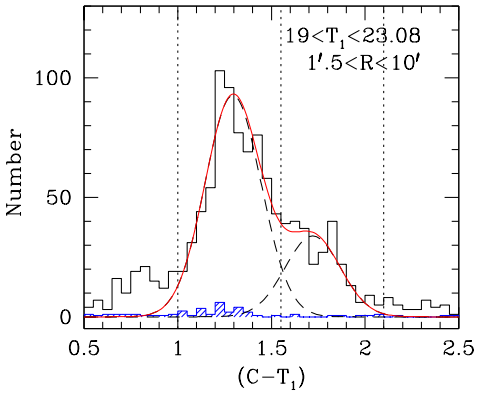

Fig. 6.— Color distribution of the M86 GCs with $19 < T_1 < 23.08$ and $1'.5 < R < 10'$. The solid line and dashed lines represent the double Gaussian fit derived from the KMM test. The hashed histogram is the color distribution of the point sources within the background region ($10' < R < 12'$). The vertical dotted lines indicate the color boundaries for the blue GCs ($1.0 < (C - T_1) < 1.55$) and the red GCs ($1.55 < (C - T_1) < 2.1$).

3.2 Color Distribution of the Globular Clusters

Fig. 6 shows the color distribution of the point sources with $19 < T_1 < 23.08$ at $1'.5 < R < 10'$ in the KPNO images. The color distribution of the background objects with the same magnitude range at $10' < R < 12'$ is also shown.

We carried out the KMM test, which estimates the statistical significance of bimodality in astronomical datasets (Ashman et al. 1994), to investigate the bimodality of the $(C - T_1)$ color distribution of the M86 GCs. KMM test of the data shows that the probability for bimodal color distribution is higher than 99.9%.

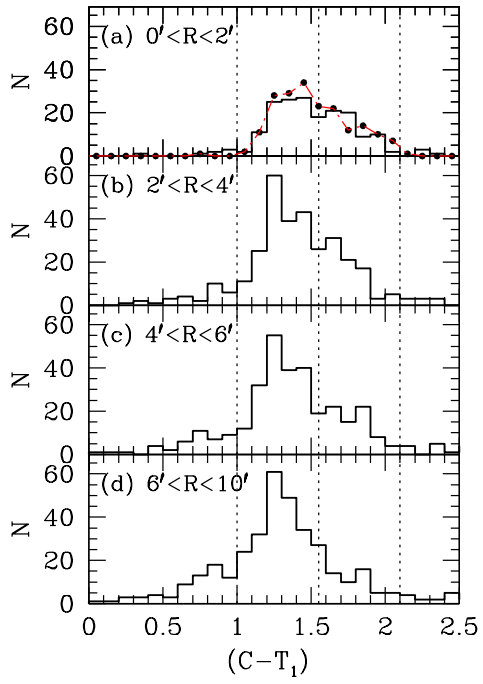

Fig. 7.— Radial color distribution of the GCs in M86. The histograms in each panel and the dot-dashed line with the circles in panel (a) represent the color distributions of the GCs obtained from KPNO and from ACSVCS catalog, respectively. The vertical dotted lines indicate the color boundaries for the sub-populations.

The color distribution is also well described as the best-fit double Gaussian curves: a blue component with center at $(C-T_1)=1.30$ and width $\sigma=0.15$ and a red component with center at $(C-T_1)=1.72$ and width $\sigma=0.15$. The minimum between the two components is found to be at $(C-T_1)\approx 1.55$. Thus we divided the entire sample of the M86 GCs into two sub-populations: the blue GCs (BGC) with $1.0<(C-T_1)<1.55$ and the red GCs (RGC) with $1.55<(C-T_1)<2.1$. This boundary color is consistent with the previous study of M86 (Rhode & Zepf 2004), but is bluer than that used for M60 (Lee et al. 2008) and M49 (Lee et al. 1998) and slightly redder than that used for M87 (Côté et al. 2001). Fig. 7 displays the radial variation of the color distribution of the M86 GCs. The number ratio of the blue GCs and the red GCs increases as the galactocentric radius increases.

3.3 Surface Photometry of M86

We derived surface photometry of M86 from the KPNO images using the IRAF/ELLIPSE task. After masking out the bright foreground stars and background galaxies and using the mode values of the regions at $R\gtrsim 10'$ in the north-east corner as the background levels, we carried out ellipse fitting to the C and T_1 images. The errors for the surface brightness magnitudes are given by ELLIPSE. The long exposure images are saturated at the central region of M86, while the short exposure images are not. Thus we used the values from the short exposure images at $R<1'$, the average values from the short and long exposure images at $1'<R<3'$, and the values from the long exposure images at $R>3'$.

Fig. 8 shows the radial profiles of the surface brightness magnitudes, $(C-T_1)$ color, ellipticity, and position angle (P. A.) of M86 as a function of major radius R_{maj}. The surface brightness profiles of the C and T_1 magnitudes are consistent with that of the B magnitude given by Caon et al. (1990). The surface brightness profiles are roughly described by a de Vaucouleurs law. These surface brightness profiles are fitted with a de Vaucouleurs $R^{1/4}$ law for the range of $2''<R_{maj}<400''$, using linear least-squares fitting: $\mu(C)=2.173(\pm0.032)R^{1/4}+16.009(\pm0.086)$ with rms=0.219, and $\mu(T_1)=2.247(\pm0.033)R^{1/4}+13.981(\pm0.089)$ with rms=0.226. The effective radius (R_{eff}) and standard radius (R_{25}) for C-band are derived to be $3'.59$ and $4'.88$ ($3'.14$ and $9'.64$ for T_1), corresponding to linear sizes of 17.54 kpc and 23.85 kpc, respectively.

This value for the effective radius is much smaller than that derived from the small field HST/ACS images by Ferrarese et al. (2006) ($R_{\rm eff}=6'.86\simeq 33.52$ kpc at g-band) but similar to that derived from wide field images by Kormendy et al. (2009) ($R_{\rm eff}=3'.38\simeq 16.52$ kpc at V-band). The surface brightness profiles of C and T_1 magnitudes in this study as well as the B magnitude given by Caon et al. (1990) show a break at $R_{maj}\sim 135''$, resulting in flatter profiles in the outer region. Thus we carried out double linear fits with $R^{1/4}$ law at $10''<R_{maj}<135''$: $\mu(C)=2.240(\pm0.016)R^{1/4}+16.027(\pm0.042)$ with rms=0.038 and $\mu(T_1)=2.304(\pm0.021)R^{1/4}+14.030(\pm0.052)$ with rms=0.047, and $135''<R_{maj}<560''$: $\mu(C)=1.706(\pm0.042)R^{1/4}+17.684(\pm0.170)$ with rms=0.063 and $\mu(T_1)=1.860(\pm0.056)R^{1/4}+15.338(\pm0.227)$ with rms=0.084.

The $(C-T_1)$ color of the M86 nucleus is very red with $(C-T_1)\approx 2.1$. It becomes rapidly bluer in the inner region ($R_{maj}\leq 50''$) as the galactocentric radius increases, but changes slowly in the outer region. This trend is consistent with the radial variation of $(U-R)$ colors given by Peletier et al. (1990) as shown in Fig. 8 (b), but is somewhat different from the $(B-R)$ colors given by Peletier et al.(1990). This may be related to the existence of dust close to the M86 center, as seen in the far-infrared images (Stickel et al. 2003; Gomez et al. 2010). The color at $2''<R_{maj}<300''$ is approximately fitted by the log-linear relation $(C-T_1)=-0.105(\pm0.003)\log R+1.999(\pm0.005)$ with rms=0.014. The ellipticity increases rapidly from 0.15 in the central region to 0.25 at $R_{maj}\approx 40''$, staying almost constant at $40''<R_{maj}<135''$. Then it increases again to ~ 0.4 in the outer region. Thus the isophotes of the outer region are more elongated than the central region.

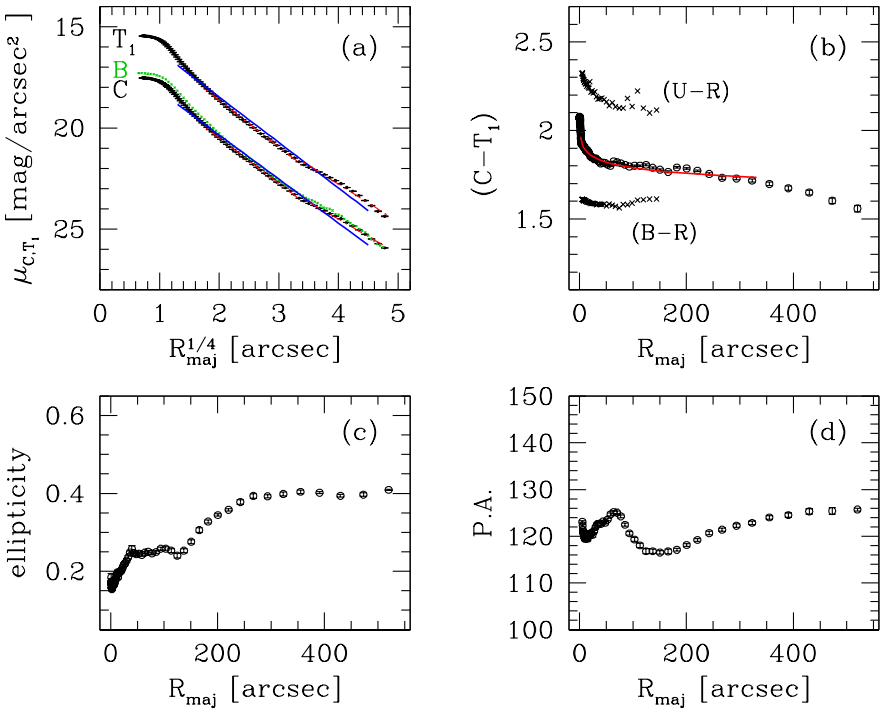

Fig. 8.— Surface photometry of M86. R_{maj} is galactocentric distance along the major axis of M86 stellar light. (a) Surface brightness magnitudes for T_1 and C. The solid lines represent the linear least-squares fits with $R^{1/4}$ law for $2'' < R_{maj} < 400''$. The dot-dashed lines represent the double linear fits with $R^{1/4}$ law for $10'' < R_{maj} < 135''$ and $135'' < R_{maj} < 560''$. The crosses indicate the surface brightness profile for B magnitude given by Caon et al. (1990). (b) Surface color profiles. The solid line indicates the power law fit of $(C - T_1)$ and $\log(R)$ for $2'' < R_{maj} < 300''$. The circles and crosses represent the colors from this study and from Peletier et al. (1990), respectively. (c) Ellipticity versus R_{maj}. (d) Position angle (P. A.) versus R_{maj}.

The values of the ellipticity at the effective radius and standard radius are 0.35 and 0.40, respectively. The value for P. A. is constant with 120 ± 6 deg.

3.4 Spatial Distribution of the Globular Clusters

We investigated the spatial structure of the M86 GC system. Fig. 9 displays the spatial distributions of the GCs with $19 < T_1 < 23.08$ mag (all GCs, blue GCs, and red GCs) as well as M86 stellar light. We also overlay number density contours of the GCs in this figure. T_1 image of M86 with isophotal contours is displayed in the panel (b) for comparison with the GC system.

Several features are noted in this figure. Firstly, all the GCs have a circular spatial distribution, and show a central concentration. Second, the blue GCs have a roughly circular spatial distribution, extended farther than the red GCs. Third, the red GCs have a spatial distribution somewhat elongated along the southeast-northwest direction, which is consistent with the distribution of M86 stellar halo. Using the dispersion ellipse method (Trumpler & Weaver 1953; Hwang & Lee 2008; Strader et al. 2011), we measured ϵ (ellipticity)$= 0.04 \pm 0.02$, 0.02 ± 0.03, and 0.16 ± 0.05, and P. A.$=122 \pm 24$, 42 ± 43, and 131 ± 10 deg for all the GCs, the blue GCs, and the red GCs at $R < 5'$, respectively. The value for the ellipticity of the red GCs is eight times larger than that of the blue GCs. The P. A.'s of all the GCs and the red GCs are similar to that of M86 stellar light.

3.5 Radial Number Density Profiles of the Globular Clusters

We derived the radial number density profiles of the GCs with $19 < T_1 < 23.08$ mag, using the KPNO results for the outer region at $R > 1'.5$ and the ACSVCS catalog for the central region at $R < 1'.5$. Here we masked out the region with $5' \times 1'.5$ centered on NGC 4402 to remove any contamination due to this galaxy. Firstly, we applied the correction for the incompleteness of photometry using the results shown in Fig. 4. Rhode & Zepf(2004) found that the radial number density of the GCs in M86 becomes zero at $R > 17'$. The field of view of our KPNO images is not wide enough to cover the entire region of M86. Here we adopted, as a background number density, a half of the number density of the point sources at $10' < R < 12'$: 0.915 ± 0.279 arcmin^{-2} for all the GCs, 0.767 ± 0.255 arcmin^{-2} for the blue GCs, and 0.149 ± 0.113 arcmin^{-2} for the red GCs. We subtracted these values from the original counts.

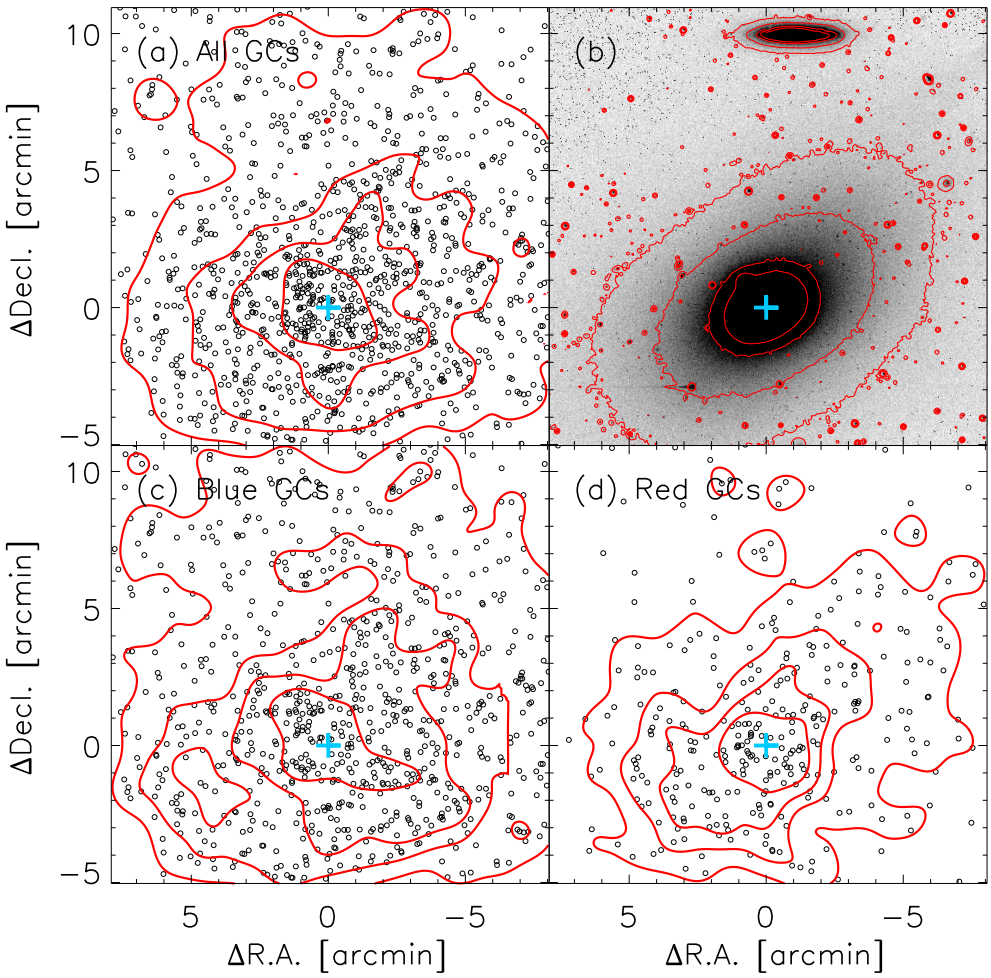

Fig. 9.— Spatial distributions and number density contours of M86 GCs. The plus signs indicate the center of the galaxy. (a) All GCs. The contour levels are 2.037, 5.093, 8.148, and 12.223 GCs arcmin^{-2}. (b) The grey map with isophotal contours in the T_1 image of M86. (c) Blue GCs. The contour levels are 0.6 times of those for all the GCs. (d) Red GCs. The contour levels are 0.4 times of those for all the GCs.

Then we derived radial number densities, considering the effect of the GC luminosity function (by multiplying by a factor of two). The radial number densities of the GCs thus derived are listed in Table 4.

Fig. 10 displays the radial number density profiles of the GCs versus $R^{1/4}$ in (a), R in (b) and (c). We also plot the radial number density profile of M86 GCs given by Rhode & Zepf (2004) and the C-band surface brightness profile of M86 in (a) for comparison. Several notable features are seen as follows. Firstly, the density profile of all the GCs is more extended than the galaxy stellar light. The density profile of all the GCs derived in this study agrees well with that given by Rhode & Zepf (2004). Secondly, the density profile of the blue GCs decreases more slowly as the galactocentric distance increases than that of the red GCs. Thirdly, the density profile of the red GCs is consistent with the surface brightness profile of the galaxy stellar light.

Fourthly, the density profiles of the GCs at $1' < R < 10'$ are approximately fitted either by a de Vaucouleurs $R^{1/4}$ law: $\log n_{GC} = -1.683(\pm0.104)R^{1/4} + 3.379(\pm0.154)$ for all the GCs, $\log n_{GC} = -1.534(\pm0.082)R^{1/4} + 3.006(\pm0.120)$ for the blue GCs, and $\log n_{GC} = -2.048(\pm0.182)R^{1/4} + 3.382(\pm0.268)$ for the red GCs; or by a power law: $\log n_{GC} = -1.343(\pm0.116)\log R + 1.783(\pm0.080)$ for all the GCs, $\log n_{GC} = -1.226(\pm0.094)\log R + 1.552(\pm0.064)$ for the blue GCs, and $\log n_{GC} = -1.628(\pm0.185)\log R + 1.434(\pm0.127)$ for the red GCs. In the case of all the GCs, the values for the slope agree well with those given by Rhode & Zepf (2004). Effective radii of all the GCs, the blue GCs, and the red GCs are derived from the de Vaucouleurs $R^{1/4}$ law fits: $15'.33$ (= 74.50 kpc), $22'.20$ (= 107.89 kpc), and $6'.99$ (= 33.97 kpc), respectively. Thus the effective radius of the red GCs is much smaller than that of the blue GCs, showing that the central concentration of the red GCs is much stronger than that of the blue GCs. The density profiles of the GCs show a break at $R \approx 4'$, resulting

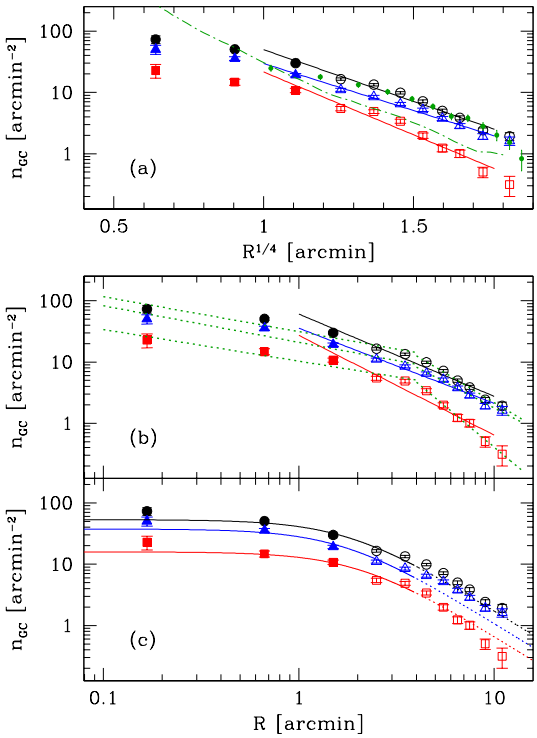

Fig. 10.— Radial number density profiles of M86 GCs. The filled and open points are from HST and KPNO, respectively. The circles, triangles, and squares represent all the GCs, the blue GCs, and the red GCs, respectively. (a) Number density versus $R^{1/4}$. The small filled circles indicate the number density profile given by Rhode & Zepf (2004). The solid lines represent the fits for a de Vaucouleurs law for $1' < R < 10'$. The dot-dashed line indicates the C surface brightness profile of the M86 stellar halo. (b) Number density versus R. The solid lines represent the fits for a power law. The dotted lines indicate the two-component power law fits for $0'.1 < R < 4'$ and $4' < R < 12'$. (c) Number density versus R. The solid lines represent King model fits for $R < 4'$, which are represented by the dotted lines for $R > 4'$.

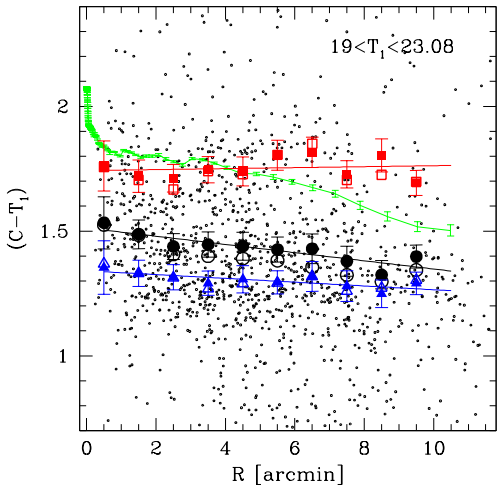

Fig. 11.— $(C - T_1)$ color of M86 GCs as a function of galactocentric distance. The circles, triangles, and squares represent all the GCs, the blue GCs, and the red GCs, respectively. The filled and open points represent mean and median color of the GCs in each radial bin, respectively. The solid lines are the linear least-squares fits about the mean color of the sub-populations. The curved line indicates $(C - T_1)$ surface color profile of M86 stellar halo.

steeper profiles in the outer region. The outer parts at $R > 4'$ are fitted well by a power law: $\log n_{GC} = -1.915(\pm0.085)\log R + 2.255(\pm0.073)$ for all the GCs, $\log n_{GC} = -1.672(\pm0.101)\log R + 1.923(\pm0.086)$ for the blue GCs, and $\log n_{GC} = -2.666(\pm0.109)\log R + 2.276(\pm0.093)$ for the red GCs. The inner parts at $R < 4'$ are fitted well by a power law: $\log n_{GC} = -0.569(\pm0.094)\log R + 1.496(\pm0.045)$ for all the GCs, $\log n_{GC} = -0.596(\pm0.100)\log R + 1.322(\pm0.047)$ for the blue GCs, and $\log n_{GC} = -0.516(\pm0.089)\log R + 1.014(\pm0.042)$ for the red GCs. In the case of the outer parts, the radial number density profile of the red GCs is much steeper than that of the blue GCs, while in the case of the inner parts, the sub-populations have similar slopes.

Finally, the density profiles of the GCs are somewhat flat in the central region at $R \lesssim 2'$. This flat radial profile, which may indicate dynamical relaxation of the GC system (Côté et al. 1998) or the relic of the GC formation epoch (Harris et al. 1998; Kundu et al. 1999), can be approximately fitted by a King model (King 1962). Fig. 10c displays the results of a King model fitting for $R < 4'$. We derived core radius $r_c = 1'.82$ and concentration parameter $c = 5.13$ for all the GCs, $r_c = 1'.71$ and $c = 5.34$ for the blue GCs, and $r_c = 2'.07$ and $c = 5.68$ for the red GCs. It is noted that in the case of the blue GCs the radial density profile of the outer region at $R > 4'$ shows an excess over the King model.

3.6 Radial Variation of Globular Cluster Colors

We investigated the radial variation of the color of the M86 GCs. Fig. 11 displays the $(C - T_1)$ colors of the GCs with $19 < T_1 < 23.08$ mag as a function of galactocentric distance derived from the KPNO images. The mean color of all the GCs in each radial bin shows a radial gradient, while those of the blue GC and the red GC show little radial gradients. The linear least-squares fitting at $R < 10'$ yields $(C - T_1) = -0.016(\pm0.003)R + 1.512(\pm0.018)$ with rms=0.026 for all the GCs, $(C - T_1) = -0.008(\pm0.002)R + 1.341(\pm0.012)$ with rms=0.017 for the blue GCs, and $(C - T_1) = 0.002(\pm0.005)R + 1.743(\pm0.028)$ with rms=0.040 for the red GCs. The color gradient of all the GCs is due to the variation of the number ratio of the blue GCs to the red GCs as shown in Fig. 7. This negative color gradient for all the GCs is consistent with the previous studies based on $(B - R)$ color (Rhode & Zepf 2004). The mean

Table 4.
Radial number density profiles of the GCs in M86

R (arcmin)	$n_{\rm AGC}$ (arcmin^{-2})	$n_{\rm BGC}$ (arcmin^{-2})	$n_{\rm RGC}$ (arcmin^{-2})
0.167	73.193 ± 10.417	50.392 ± 8.668	22.800 ± 5.778
0.667	50.465 ± 3.066	35.706 ± 2.588	14.758 ± 1.644
1.500	29.959 ± 1.487	19.182 ± 1.201	10.776 ± 0.877
2.500	16.475 ± 0.755	11.020 ± 0.626	5.455 ± 0.423
3.500	13.403 ± 0.589	8.506 ± 0.478	4.897 ± 0.343
4.500	9.894 ± 0.454	6.498 ± 0.376	3.394 ± 0.254
5.500	7.169 ± 0.383	5.191 ± 0.332	1.979 ± 0.192
6.500	4.993 ± 0.324	3.761 ± 0.285	1.232 ± 0.153
7.500	3.854 ± 0.286	2.849 ± 0.252	1.006 ± 0.137
9.000	2.422 ± 0.224	1.917 ± 0.202	0.505 ± 0.097
11.000	1.927 ± 0.279	1.614 ± 0.255	0.314 ± 0.113

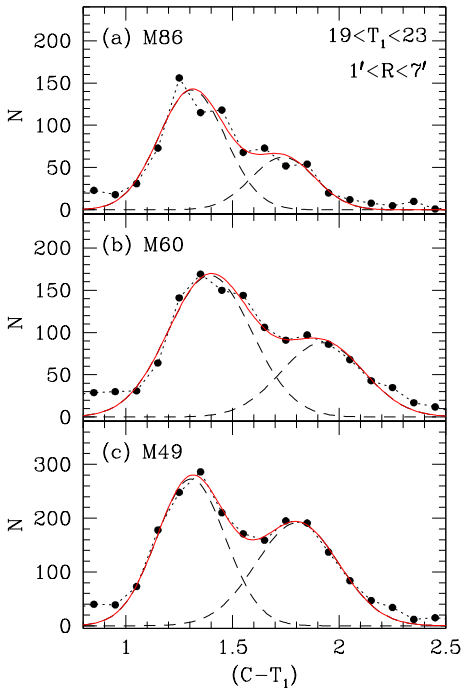

Fig. 12.— Comparison of the color distribution between the GCs in M86 and the GCs in other Virgo gEs. (a) M86 from this study. (b) M60 from Lee et al. (2008). (c) M49 from Geisler (1996) and Lee et al.(1998). The solid and dashed lines represent the double Gaussian fits.

color of the M86 stellar light is much closer to that of the red GCs than to that of the blue GCs, as often seen in other gEs such as M49 and M60 (Lee et al. 1998; Lee et al. 2008).

4. DISCUSSION

We compared the photometric results of the M86 GC system with those of GC systems in other two gEs in Virgo (M60 and M49). M60, which is the third brightest gE in Virgo and located about 3 deg from the Virgo center, and M49, which is the brightest gE in Virgo and located about 4 deg from the Virgo center. Previous studies for the GC systems of M60 (Lee et al. 2008) and M49 (Geisler et al. 1996; Lee et al. 1998) used the same instruments and similar photometric techniques as this study for the M86 GC system. For comparison we used the same criteria for the GC sample in three galaxies, GCs with $R < 7'$ and $19 < T_1 < 23$.

Fig. 12 displays the color distributions of the GCs in M86, M60, and M49. The GCs in these galaxies show similar bimodal color distributions, but there are slight differences among these galaxies. The peak colors for M86 ($(C - T_1) = 1.31$ and 1.74) are similar to those for M49 ($(C - T_1) = 1.30$ and 1.79), but are about 0.1 mag bluer than those for M60 ($(C - T_1) = 1.37$ and 1.87). Applying this color difference to the relation between $(C-T_1)$ color and metallicity (Lee et al. 2008), this implies that the M86 and the M49 GCs are on average about 0.2 dex more metal-poor than M60 GCs. These results are approximately consistent with those by Peng et al. (2006) who covered the central regions with $R \lesssim 1'.5$. They reported that the peak colors for these three galaxies are $(g-z) = 0.98$ and 1.33 for M86, $(g - z) = 0.97$ and 1.42 for M49, and $(g - z) = 0.98$ and 1.45 for M60.

There are significant differences among the number ratios (N(BGC)/N(RGC)) of the blue GCs to the red GCs in these galaxies: 2.37 ± 0.26 for M86, 1.38 ± 0.11 for M60, and 0.97 ± 0.07 for M49. Thus the fraction of the blue GCs for M86, the faintest among these three galaxies, is the largest. This is consistent with

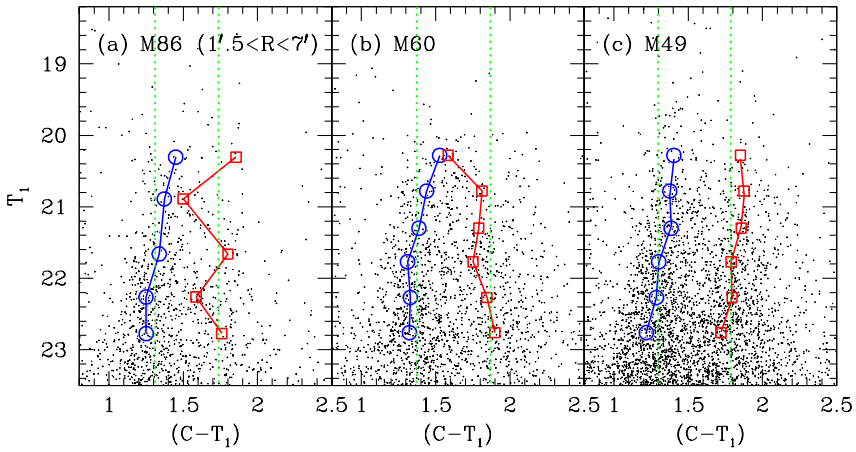

Fig. 13.— Comparison of the CMDs for the GCs in the Virgo gEs with $1'.5 < R < 7'$. (a) M86. (b) M60. (c) M49. The vertical dotted lines indicate the peak values of the blue GCs and the red GCs with $19 < T_1 < 23$. The large open circles and squares represent the peak values in each magnitude bin derived from the KMM test.

the previous finding that the fraction of the blue GCs decreases as their host galaxy gets brighter (Peng et al. 2006). On the other hand, the number ratio of the blue GCs to the red GCs in each galaxy is a little bit larger than the value by Peng et al. (2006). (2.33 ± 1.15 for M86, 0.75 ± 0.10 for M60, and 0.69 ± 0.09 for M49) and by Faifer et al. (2011)(1.07 ± 0.10 for M60). The radial coverages used by Peng et al. (2006) and Faifer et al. (2011) are $R \lesssim 1'.5$ and $R \lesssim 5'$, respectively, so that their fields are on average closer to the galaxy center than that used in this study ($1' < R < 7'$). These show that this number ratio decreases as the galactocentric radius decreases (see section 3.2 for detail).

Recent studies for the GCs in gEs based on HST/ACS data (Harris et al. 2006; Strader et al. 2006; Mieske et al. 2006; Peng et al. 2009; Mieske et al. 2010) and wide-field images (Forte et al. 2007; Lee et al. 2008; Harris 2009a), found a so-called 'blue tilt' (or a color-magnitude relation): the brighter the bright blue GCs are, the redder their colors get. Several mechanisms were proposed to explain the origin of the blue tilt (Mieske et al. 2006; Bekki et al. 2007; Strader & Smith 2008; Harris 2009b; Blakeslee et al. 2010). The self-enrichment process among these appears to be the main driver (Mieske et al. 2006; Strader & Smith 2008). We investigated for any existence of this blue tilt in the M86 GCs. Fig. 13 displays the CMDs of M86, M60, and M49 derived from the CT_1 images for the outer regions at $1'.5 < R < 7'$. The blue and red peak values are determined from the KMM test with the colors in each magnitude bin. In Fig. 13 the blue tilt is seen for the bright blue GCs in M86 as well as other two galaxies. However, the number of galaxies is only three so that we need to study more galaxies to address the slope difference of the blue tilt. The existence of the blue tilt in M86 as well as M49 and M60 is consistent with the result for high mass galaxies in the ACSVCS given by Mieske et al. (2010).

The spatial distribution of the GCs in three galaxies share common features as follows: (a) the radial number density profile of the red GCs in the outer region is consistent with the surface brightness profile of the stellar halo, (b) the elongation of the red GC system is consistent with that of the stellar halo, while the spatial distribution of the blue GC system is approximately circular, (c) the mean color of the red GCs is similar to that of the stellar halo. These common properties are also shown for other gE GC systems such as M87 and NGC 1399 (Bassino et al. 2006; Tamura et al. 2006; Forte et al. 2007; Faifer et al. 2011; Strader et al. 2011; Forte et al. 2012). Thus the red GCs are more correlated with the stellar halo than the blue GCs. This indicates that most red (metal-rich) GCs in gEs might have formed with the halo stars.

5. SUMMARY

We have presented Washington CT_1 photometry of the GCs in M86 covering a $16' \times 16'$ field and showed various photometric properties of the GC system. Primary results are summarized as follows.

1. A significant population of GCs in M86 are shown in the CMD.
2. The color distribution of the GCs in M86 is bimodal, showing a blue peak at $(C-T_1) = 1.30$ and width $\sigma = 0.15$, and a red peak at $(C-T_1) = 1.72$ and $\sigma = 0.15$, with a division color $(C - T_1) \approx 1.55$.
3. The spatial distribution of the blue GCs is roughly circular, while that of the red GCs is elongated similar to that of the stellar halo.
4. The radial number density profile of M86 GC system is more extended than the galaxy stellar light. The radial density profile of the red GCs is consistent with the surface brightness profile of M86

stellar halo. The radial density profile of the blue GCs is more extended than that of the red GCs. The density profiles at $1' < R < 10'$ are approximately well fitted by a de Vaucouleurs law and a power law. As a result, the slope of the radial profile of the red GCs is steeper than that of the blue GCs. The radial density profiles in the central region are somewhat flat and approximately fitted by a King model.

5. M86 GCs have the negative radial color gradient because the number ratio of the blue GCs to the red GCs increases as galactocentric radius increases. The mean color of the red GCs is similar to that of the stellar halo.
6. As seen in other Virgo gEs, the bright blue GCs in the outer region of M86 reveal a blue tilt that the mean colors of the blue GCs get redder as they get brighter.

ACKNOWLEDGMENTS

The author is grateful to his collaborators: Profs. Myung Gyoon Lee and Doug Geisler. This is supported in part by Mid-career Researcher Program through NRF grant funded by the MEST (No.2010-0013875).

REFERENCES

Ashman, K. M., Bird, C. M., & Zepf, S. E. 1994, Detecting Bimodality in Astronomical Datasets, AJ, 108, 2348

Bassino, L. P., Faifer, F. R., Forte, J. C., Dirsch, B., Richtler, T., Geisler, D., & Schuberth, Y. 2006, Large-Scale Study of the NGC 1399 Globular Cluster System in Fornax, A&A, 451, 789

Bekki, K., Yahagi, H., & Forbes, D. A. 2007, On the Origin of Mass-Metallicity Relations, Blue Tilts and Scaling Relations for Metal-poor Globular Cluster Systems, MNRAS, 377, 215

Blakeslee, J. P., Cantiello, M., & Peng, E. W. 2010, The Mass-Metallicity Relation of Globular Clusters in the Context of Nonlinear Color-Metallicty Relations, ApJ, 710, 51

Brodie, J. P., & Strader, J. 2006, Extragalactic Globular Clusters and Galaxy Formation, ARA&A, 44, 193

Caon, N., Capaccioli, M., & Rampazzo, R. 1990, Photographic and CCD Surface Photometry of 33 Early-type Galaxies in the Virgo Cluster, A&AS, 86, 429

Cohen, J. G. 1988, The Globular Cluster Systems of the Three Virgo Ellipticals, AJ, 95, 682

Côté, P., Marzke, R. O., & West, M. J. 1998, The Formation of Giant Elliptical Galaxies and Their Globular Cluster Systems, ApJ, 501, 554

Côté, P., McLaughlin, D. E., Hanes, D. A., Bridges, T. J., Geisler, D., Merritt, D., Hesser, J. E., Harris, G. L. H., & Lee, M. G. 2001, Dynamics of the Globular Cluster System Associated with M87 (NGC 4486). II. Analysis, ApJ, 559, 828

de Vaucouleurs, G., de Vaucouleurs, A., Corwin, H. G. Jr., Buta, R. J., Paturel, H. G., & Fouqué, P. 1991, Third Reference Catalog of Bright Galaxies (New York: Springer)

Dirsch, B., Schuberth, Y., & Richtler, T. 2005, A Wide-Field Photometric Study of the Globular Cluster System of NGC 4636, A&A, 433, 43

Faifer, F. R., Forte, J. C., Norris, M. A., Bridges, T., Forbes, D. A., Zepf, S. E., Beasley, M., Gebhardt, K., Hanes, D. A., & Sharples, R. M. 2011, Gemini/GMOS Imaging of Globular Cluster Systems in Five Early-Type Galaxies, MNRAS, 416, 155

Ferrarese, L., Côté, P., Jordán, A., Peng, E. W., Blakeslee, J. P., Piatek, S., Mei, S., Merritt, D., Milosavljević, M., Tonry, J. L., & West, M. J. 2006, The ACS Virgo Cluster Survey. VI. Isophotal Analysis and the Structure of Early-Type Galaxies, ApJS, 164, 334

Forte, J. C., Faifer, F., & Geisler, D. 2007, A Quantitative Link between Globular Clusters and the Stellar Haloes in Elliptical Galaxies, MNRAS, 382, 1947

Forte, J. C., Vega, E. I., & Faifer, F. 2012, Mapping the Galaxy NGC 4486 (M87) through its Globular Cluster System, MNRAS, 421, 635

Geisler, D. 1996, New Washington System CCD Standard Fields, AJ, 111, 480

Geisler, D., & Forte, J. 1990, The Abundance Distribution and Luminosity Function of Globular Clusters in NGC 1399, ApJ, 350, L5

Geisler, D., Lee, M. G., & Kim, E. 1996, Washington Photometry of the Globular Cluster System of NGC 4472.I.Analysis of the Metallicities, AJ, 111, 1529

Gomez, H. L., Baes, M., Cortese, L., Smith, M. W. L., Boselli, A., Ciesla, L., Bendo, G. J., Pohlen, M., di Serego Alighieri, S., Auld, R., & 51 coauthors. 2010, The Dust Morphology of the Elliptical Galaxy M86 with SPIRE, A&A, 518, L45

Hanes, D. A. 1977, The Luminosity Distribution of Globular Clusters in the Virgo Cluster of Galaxies, MmRAS, 84, 45

Harris, W. E., Harris, G. L. H., & McLaughlin, D. E. 1998, M87, Globular Clusters, and Galactic Winds: Issues in Giant Galaxy Formation, AJ, 115, 1801

Harris, G. L. H., Harris, W. E., & Geisler, D. 2004, Wide-Field Washington Photometry of the NGC 5128 Globular Cluster System. II. Large-Scale Properties of the System, AJ, 128, 723

Harris, W. E., Whitmore, B. C., Karakla, D., Okon, W., Baum, W. A., Hanes, D. A., & Kavelaars, J. J.

2006, Globular Cluster Systems in Brightest Cluster Galaxies: Bimodal Metallicity Distributions and the Nature of the High-Luminosity Clusters, ApJ, 636, 90

Harris, W. E. 2009a, The Globular Cluster System in M87: A Wide-Field Study with CFHT/Megacam, ApJ, 703, 939

Harris, W. E. 2009b, Globular Cluster Systems in Giant Ellipticals: The Mass/Metallicity Relation, ApJ, 699, 254

Hwang, H. S., & Lee, M. G. 2008, Galaxy Orbits for Galaxy Clusters in the Sloan Digital Sky Survey and Two Degree Field Galaxy Redshift Survey, ApJ, 676, 218

Jordań, A., McLaughlin, D. E., Ferrarese, L., Peng, E. W., Mei, S., Villegas, D., Merritt, D., Tonry, J. L., & West, M. J. 2007, The ACS Virgo Cluster Survey. XII. The Luminosity Function of Globular Clusters in Early-Type Galaxies, ApJS, 171, 101

Jordán, A., Peng, E. W., Blakeslee, J. P., Côté, P., Eyheramendy, S., Ferrarese, L., Mei, S., Tonry, J. L., & West, M. J. 2009, The ACS Virgo Cluster Survey XVI. Selection Procedure and Catalogs of Globular Cluster Candidates, ApJS, 180, 54

King, I. 1962, The Structure of Star Clusters. I. An Empirical Density Law, AJ, 67, 471

Kormendy, J., Fisher, D. B., Cornell, M. E., & Bender, R. 2009, Structure and Formation of Elliptical and Spheroidal Galaxies, ApJS, 182, 216

Kron, R. 1980, Photometry of a Complete Sample of Faint Galaxies, ApJS, 43, 305

Kundu, A., Whitmore, B. C., Sparks, W. B., Macchetto, F. D., Zepf, S. E., & Ashman, K. M. 1999, The Globular Cluster System in the Inner Region of M87, AJ, 121, 2950

Kundu, A., & Whitmore, B. C. 2001, New Insights from HST Studies of Globular Cluster Systems. I. Colors, Distances, and Specific Frequencies of 28 Elliptical Galaxies, AJ, 121, 2950

Larsen, S. S., Brodie, J. P., Huchra, J. P., Forbes, D. A., & Grillmair, C. J. 2001, Properties of Globular Cluster Systems in Nearby Early-Type Galaxies, AJ, 121, 2974

Lee, M. G. 2003, On the Formation of Giant Elliptical Galaxies and Globular Clusters, JKAS, 36, 18

Lee, M. G., Kim, E., & Geisler, D. 1998, Washington Photometry of the Globular Cluster System of NGC 4472. II. The Luminosity Function and Spatial Structure, AJ, 115, 947

Lee, M. G., Park, H. S., Kim, E., Hwang, H. S., Kim, S. C., & Geisler, D. 2008, Washington CCD Photometry of the Globular Cluster System of the Giant Elliptical Galaxy M60 in Virgo, ApJ, 682, 135

Mei, S., Blakeslee, J. P., Côté, P., Tonry, J. L., West, M. J., Ferrarese, L., Jordán, A., Peng, E. W., Anthony, A., & Merritt, D. 2007, The ACS Virgo Cluster Survey. XIII. SBF Distance Catalog and the Three-dimensional Structure of the Virgo Cluster, ApJ, 655, 144

Mieske, S., Jordán, A., Côté, P., Kissler-Patig, M., Peng, E. W., Ferrarese, L., Blakeslee, J. P., Mei, S., Merritt, D., Tonry, J. L., & West, M. J. 2006, The ACS Virgo Cluster Survey. XIV. Analysis of Color-Magnitude Relations in Globular Cluster Systems, ApJ, 653, 193

Mieske, S., Jordán, A., Côté, P., Peng, E. W., Ferrarese, L., Blakeslee, J. P., Mei, S., Baumgardt, H., Tonry, J. L., Infante, L., & West, M. J. 2010, The ACS Fornax Cluster Survey. IX. The Color-Magnitude Relation of Globular Cluster Systems, ApJ, 710, 1672

Neilsen, E. H., Jr., & Tsvetanov, Z. I. 1999, The Color Distributions of Globular Clusters in Virgo Elliptical Galaxies, ApJ, 515, L13

Peletier, R. F., Davies, R. L., Illingworth, G. D., Davis, L. E., & Cawson, M. 1990, CCD Surface Photometry of Galaxies with Dynamical Data. II - UBR Photometry of 39 Elliptical Galaxies, AJ, 100, 1091

Peng, E. W., Jordán, A., Côté, P., Blakeslee, J. P., Ferrarese, L., Mei, S., West, M. J., Merritt, D., Milosavljević, M., & Tonry, J. L. 2006, The ACS Virgo Cluster Survey. IX. The Color Distributions of Globular Cluster Systems in Early-Type Galaxies, ApJ, 639, 95

Peng, E. W., Jordán, A., Côté, P., Takamiya, M., West, M. J., Blakeslee, J. P., Chen, C.-W., Ferrarese, L., Mei, S., Tonry, J. L., & West, A. A. 2008, The ACS Virgo Cluster Survey. XV. The Formation Efficiencies of Globular Clusters in Early-Type Galaxies: The Effects of Mass and Environment, ApJ, 681, 197

Peng, E. W., Jordán, A., Blakeslee, J. P., Mieske, S., Côté, P., Ferrarese, L., Harris, W. E., Madrid, J. P., & Meurer, G. R. 2009, The Color-Magnitude Relation for Metal-Poor Globular Clusters in M87: Confirmation from Deep HST/ACS Imaging, ApJ, 703, 42

Rhode, K. L., & Zepf, S. E. 2004, The Globular Cluster Systems of the Early-Type Galaxies NGC 3379, NGC 4406, and NGC 4594 and Implications for Galaxy Formation, AJ, 127, 302

Schlegel, D. J., Finkbeiner, D. P., & Davis, M. 1998, Maps of Dust Infrared Emission for Use in Estimation of Reddening and Cosmic Microwave Background Radiation Foregrounds, ApJ, 500, 525

Smith, R. J., Lucey, J. R., Hudson, M. J., Schlegel, D. J., & Davies, R. L. 2000, Streaming Motions of Galaxy Clusters within 12000 kms^{-1} - I. New Spectroscopic Data, MNRAS, 313, 469

Stickel, M., Bregman, J. N., Fabian, A. C., White, D. A., & Elmegreen, D. M. 2003, Deep ISOPHOT Far-Infrared Imaging of M86, A&A, 397, 503

Strader, J., Brodie, J. P., Spitler, L., & Beasley, M. A. 2006, Globular Clusters in Virgo Ellipticals: Unexpected Results for Giants and Dwarfs from Advanced Camera for Surveys Imaging, AJ, 132, 2333

Strader, J., & Smith, G. H. 2008, The Origin of the Blue Tilt in Extragalactic Globular Cluster Systems, AJ, 136, 1828

Strader, J., Romanowsky, A. J., Brodie, J. P., Spitler, L. R., Beasley, M. A., Arnold, J. A., Tamura, N., Sharples, R. M., & Arimoto, N. 2011, Wide-field Precision Kinematics of the M87 Globular Cluster System, ApJS, 197, 33

Stetson, P. B. 1994, The Center of the Core-Cusp Globular Cluster M15: CFHT and HST Observations, ALLFRAME Reductions, PASP, 106, 250

Tamura, N., Sharples, R. M., Arimoto, N., Onodera, M., Ohta, K., & Yamada, Y. 2006, A Subaru/Suprime-Cam Wide-Field Survey of Globular Cluster Populations around M87 - II. Colour and Spatial Distribution, MNRAS, 373, 601

Trumpler R. J., & Weaver H. F. 1953, Statistical Astronomy (Berkeley: Univ. California Press)

Villegas, D., Jordán, A., Peng, E. W., Blakeslee, J. P., Côté, P., Ferrarese, L., Kissler-Patig, M., Mei, S., Infante, L., Tonry, J. L., & West, M. J. 2010, The ACS Fornax Cluster Survey. VIII. The Luminosity Function of Globular Clusters in Virgo and Fornax Early-Type Galaxies and Its Use as a Distance Indicator, ApJ, 717, 603